

Superior Electrocatalyst for All-pH Hydrogen Evolution Reaction: Heterogeneous Rh/N and S Co-Doped Carbon Yolk–Shell Nanospheres

Xiuming Bu, Yu Bu, Quan Quan, Siwei Yang, You Meng, Dong Chen, Zhengxun Lai, Pengshan Xie, Di Yin, Dengji Li, Xianying Wang,* Jian Lu,* and Johnny C. Ho*

Design of efficient and robust electrocatalysts for hydrogen evolution reaction (HER) under all pH conditions has attracted significant attention. In particular, it is still a considerable challenge since the HER kinetics of Pt in alkaline solutions is about two to three orders of magnitude lower than that in acidic conditions. Herein, a heterogeneous yolk–shell nanostructure with Rh nanoparticles embedded in S, N co-doped carbon nanospheres prepared by a facile self-template method is reported. The optimized electrocatalyst can achieve an extremely small overpotential of 13.5 mV at 10 mA cm⁻², low Tafel slope of 25.5 mV dec⁻¹, high turnover frequency of 0.143 s⁻¹ (at -75 mV vs. reversible hydrogen electrode), and long-term durability for 10 h, which is the record-high alkaline HER activity among the ever-reported noble metal based catalysts. These striking performances are ascribed to the optimized electronic structure and unique heterogeneous yolk–shell nanostructure. More importantly, it is also demonstrated that the obtained electrocatalyst exhibits superior activities in all pH range, which is better than commercial Pt/C and Rh/C catalysts. This work proves that Rh-based nanomaterials are promising superior electrocatalysts in a wide pH range and nanostructure design is a powerful tool to increase the mass/electron transfer during reaction.

1. Introduction

Electrochemical water splitting to hydrogen powered by using renewable energy sources, instead of fossil fuels, is widely considered as one of the promising high energy density carriers for clean power in future.^[1–4] By now, Pt-based nanomaterials have served as the most effective electrocatalysts for hydrogen evolution reaction (HER) due to its hydrogen adsorption free energy (ΔG_{H}) being close to zero, requiring only a small overpotential to produce hydrogen.^[5] However, the poor stability and unsatisfied performance of Pt in non-acidic conditions greatly hinder its widespread practical applications. It is particular that an effective HER electrocatalyst is necessary to perform well in a wide pH range because of the different requirements in different electrolyzer systems, such as acidic media for proton-exchange membrane-based water electrolyzers,^[6] near-neutral media for microbial electrolysis cells¹ and alkaline

X. M. Bu, Q. Quan, Y. Meng, D. Chen, Z. X. Lai, P. S. Xie, D. Yin, D. J. Li, J. C. Ho

Department of Materials Science and Engineering
City University of Hong Kong
Hong Kong SAR 999077, P. R. China
E-mail: johnnyho@cityu.edu.hk

Y. Bu, J. Lu
Centre for Advanced Structural Materials
Shenzhen Research Institute
City University of Hong Kong
Shenzhen 518057, P. R. China
E-mail: jian.lu@cityu.edu.hk

S. W. Yang
Joint Laboratory of Graphene Materials and Applications
State Key Laboratory of Functional Materials for Informatics
Shanghai Institute of Microsystem and Information Technology
Chinese Academy of Sciences
Shanghai 200050, P. R. China

X. Y. Wang
Energy Materials Research Center AG Hydrogen Materials & Devices
CAS Key Laboratory of Materials for Energy Conversion
Shanghai Institute of Ceramics
Chinese Academy of Sciences (SICCAS)
Shanghai 200050, P. R. China
E-mail: wangxianying@mail.sic.ac.cn

J. C. Ho
State Key Laboratory of Terahertz and Millimeter Waves
City University of Hong Kong
Hong Kong SAR 999077, P. R. China

J. C. Ho
Key Laboratory of Advanced Materials Processing & Mold
Zhengzhou University
Ministry of Education
Zhengzhou 450002, P. R. China

 The ORCID identification number(s) for the author(s) of this article can be found under <https://doi.org/10.1002/adfm.202206006>.

DOI: 10.1002/adfm.202206006

media for alkaline electrolyzers,^[7] as well as the intense local pH change on the electrode surface during reaction.^[8,9] Although tremendous effects have been devoted to develop pH-universal electrocatalysts with high electrochemical performance and robust stability, even in terms of the current density calculated based on geometric surface (electrode surface area), very few of them can achieve comparable activities to commercial Pt/C electrodes.^[10,11] In this regard, it is still challenging to develop pH-universal electrocatalysts with HER activities and stability that exceed those of commercial Pt/C materials.

Combining the previous experimental results and theoretically calculated ΔG_{H} values, Rh-based nanomaterials may serve as a promising candidate for pH-universal HER electrocatalysts.^[12,13] For example, Guo and his team reported the successful preparation of monodisperse Rh₂P nanoparticles by the colloidal method, in which the nanoparticles showed excellent HER performance in a wide pH range.^[14] In addition, Du et al. used the laser ablation method to synthesize compressed RhO₂ clusters embedded in Rh nanoparticles; the impressive performance indicated that Rh-based noble metals are superior for alkaline HER.^[15] Nevertheless, the preparation methods/techniques employed are complex and time-consuming. Meanwhile, it should be noted that the ΔG_{H} value of volcano plots in hydrogen electrocatalysis is not a sufficient descriptor for intrinsic activities of electrocatalysts, since ΔG of some non-metal phosphides and sulfides are also located at the top of volcano but their HER performance is still lower than those of noble metal based electrocatalysts.^[16] One of the main reasons could be attributed to the kinetic barrier, mainly associated with the low mass and electron transfer ability on the electrocatalyst surface during reaction, limited the electrocatalytic performance.^[17,18]

Inspired by these ideas, in this work, we report an efficient and durable electrocatalyst of Rh/N,S co-doped carbon yolk-shell nanospheres (denoted as Rh/NSC YSS) via a facile self-template synthesis method for all-pH HER. The prepared electrocatalyst exhibits superior performance to most of state-of-the-art HER electrocatalysts at all pH ranges, especially in alkaline conditions. Rh/NSC YSS only requires an extremely small overpotential of 13.5 mV at 10 mA cm⁻² with a low Tafel slope of 25.5 mV dec⁻¹, high turnover frequency (TOF) of 0.143 s⁻¹ (at -75 mV per RHE) and long-term durability for 10 h, which is the best alkaline HER activity among the ever-reported noble metal based catalysts to the best of our knowledge. Importantly, the observed underpotential deposition hydrogen (H_{upd}) and gas bubbles generation/desorption behaviors have evidently proved the excellent intrinsic activities of Rh/NSC YSS coming from the optimized binding energies of hydrogen intermediates and unique heterogeneous yolk-shell nanostructure design, which accelerates the HER kinetics and gas bubbles transfer during reaction. All these results demonstrate that Rh based nanomaterials is a promising superior electrocatalyst for a wide pH range while nanostructure design is a powerful tool to enhance the mass/electron transfer during reaction.

2. Results and Discussion

The preparation process of the Rh₁₅/NSC YSS electrocatalyst (15 mg of RhCl₃ used) was conducted with a self-template

method as shown in **Figure 1a**. The Rh₁₅/NSC YSS precursor was first obtained with the nanosphere structure through a facile hydrothermal method by using RhCl₃ and thiourea as the Rh, N, S and, C sources (Figure S1, Supporting Information). Then, the precursor was in situ transformed into Rh₁₅/NSC YSS by a heat treatment in air atmosphere. As illustrated in the X-ray diffraction (XRD) pattern (Figure S2, Supporting Information), the crystallographic structure of the obtained final product can be matched well with the standard pattern of cubic Rh phase (*JCPDS NO.* 87-0714). The typical scanning electron microscopy (SEM) image of Rh₁₅/NSC YSS is shown in Figure 1b–d. The average size and shell thickness of Rh₁₅/NSC YSS is 145.1 ± 4.4 nm (Figure 1e) and 77 ± 0.1 nm (Figure 1f), respectively. The interior structure of as obtained Rh₁₅/NSC YSS was further elucidated by TEM (Figure 1g,h). A representative interplanar spacing of 0.22 nm is revealed in the HRTEM image (Figure 1i), suggesting the association with (111) plane of the cubic Rh phase. It should be noted several atomic layers of RhO₂ (with the lattice spacing of 0.17 nm corresponding to (211) plane of RhO₂, *JCPDS NO.* 43-1026) was observed on the surface of Rh₁₅/NSC YSS. The presence of carbon can be confirmed by Raman spectrum (Figure S3, Supporting Information). The ratio between the D (1350 cm⁻¹) and G band (1580 cm⁻¹) intensities ($I_{\text{D}}/I_{\text{G}}$) is 1.13, implying the presence of partial graphitization and many structural defects on the carbon shells, thus favoring electroconductivity and H⁺/H₂ absorption.^[19] The high-angle annular dark field (HAADF) STEM image clearly proves the porosity and heterogeneity, and the core has a higher Rh content compared to the shell (Figure 1j). The atomic ratio of Rh and S obtained on the grinded Rh₁₅/NSC YSS can also support the heterogeneous composition of the YSS structure (Figure S4, Supporting Information). Elemental mappings of Rh₁₅/NSC YSS in Figure 1k–n indicate that C, Rh, S, and N elements are unevenly distributed on the catalyst surface.

To shed light on the underlying mechanism for the formation of yolk-shell structure with self-template method, Rh₅/NSC and Rh₃₀/NSC electrocatalysts were prepared through changing the mass ratio between RhCl₃ and thiourea (Figure S5, Supporting Information), and the mass content of Rh in Rh₅/NSC, Rh₁₅/NSC and Rh₃₀/NSC is found to be 77.4, 82.1, and 85.2 wt%, respectively (Figure S6, Supporting Information). As shown in **Figure 2a,b**, Rh₅/NSC exhibits a typical sphere-like nanoparticle (NP) morphology with a size of 290 ± 1.9 nm (Figure S7, Supporting Information). The HRTEM image and corresponding EDS mapping reveal that the Rh atoms are evenly distributed on the N, S co-doped carbon surface (Figure 2c,d). When the Rh mass was increased, porous nanoparticles (PP) with a size of 42.5 ± 0.7 nm were obtained (Figure 2e,f; Figure S8, Supporting Information). The HRTEM and corresponding EDS mapping suggest that the increased Rh content did not change the chemical composition of the product (Figure 2g,h). Figure 2i shows the relationship between particle size and Rh/C ratio. Obviously, when the Rh/C ratio was increased, the particle size would decrease exponentially, fitting well with the Von Weimarn equation (detailed explanation shown in Note S1, Supporting Information). It should be noted here, when the Rh/C ratio is 10 (Rh₁₀/NSC) and 20 (Rh₂₀/NSC), the prepared electrocatalysts still show the yolk-shell structure (Figures S9 and S10, Supporting Information). Combined with the FT-IR spectra (Figure S11, Supporting Information), the sharp peak around

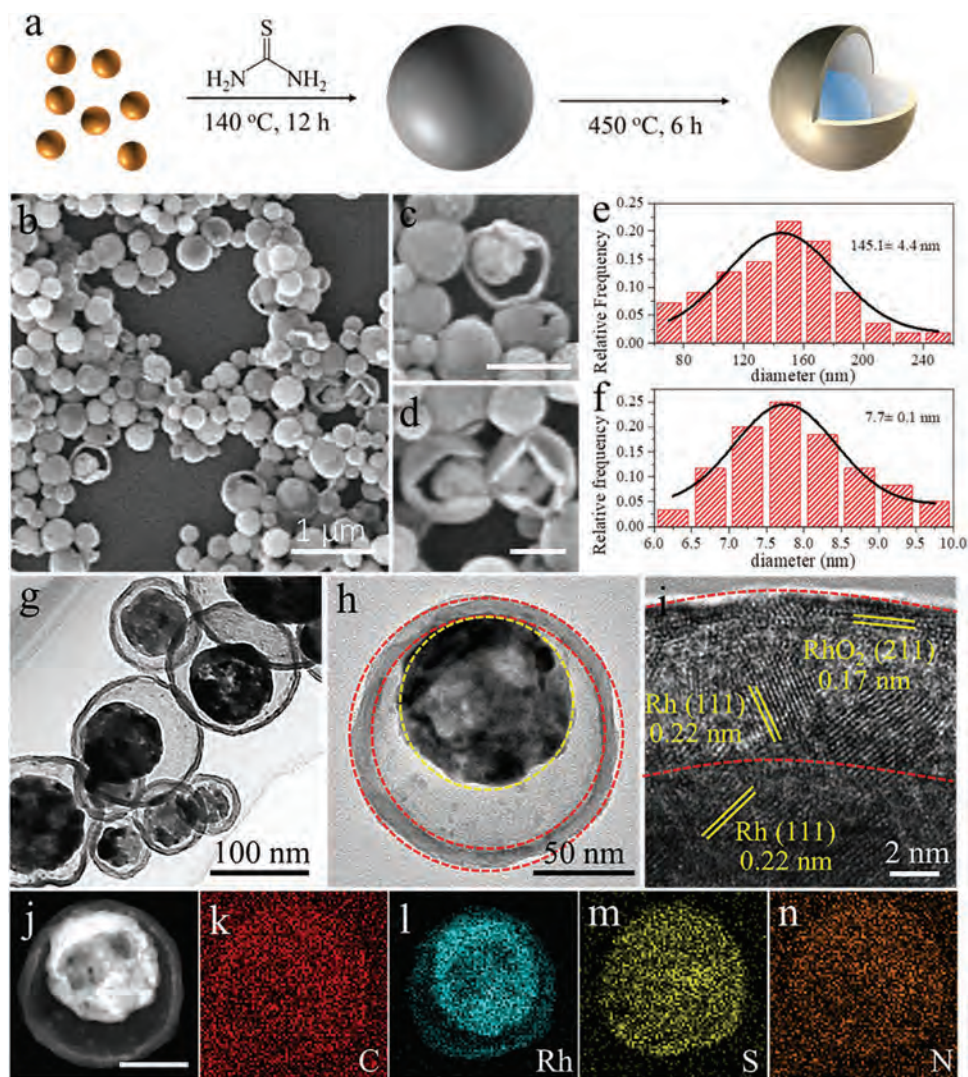


Figure 1. a) Schematic diagram of the preparation of Rh₁₅/NSC YSS electrocatalysts. Orange colored balls stand for Rh³⁺ while grey colored balls refer to the precursor of Rh₁₅/NSC YSS; b–d) SEM image of the Rh₁₅/NSC YSS catalyst. The scale bars in (c) and (d) are both 100 nm; (e) and (f) are the statistics on size distribution and shell thickness distribution of the catalysts, respectively; g,h) TEM images of the Rh₁₅/NSC YSS catalyst with different magnification; i) HRTEM image of the Rh₁₅/NSC YSS catalyst and j–n) high-angle annular dark field (HAADF) STEM image and corresponding elemental mapping of C, Rh, S, and N of the Rh₁₅/NSC YSS catalyst, respectively. The scale bar in (j) is 50 nm.

611 cm⁻¹ is caused by Rh–S(O), indicating the strong electronic effect between Rh and S, N co-doped carbon.^[20] Based on the above characterization, the possible formation mechanism of Rh/NSC is proposed (Figure 2j): I) when the Rh/C mass ratio is low, the copolymerization reaction between Rh³⁺ ions and thiourea dominates the reaction (Figure S12, Supporting Information). In this case, thiourea can get into carbon nanospheres in the presence of Rh³⁺ ions under high temperature and pressure until the Rh³⁺ ions are consumed completely. It is also noted that there would be no product obtained if only thiourea is involved in the hydrothermal reaction. II) When the Rh/C mass ratio increases, Rh³⁺ ions tend to perform homogeneous nucleation because of the positive redox potential of Rh³⁺. Therefore, in the initial stage, the homogeneous nucleation of Rh³⁺ ions dominates the reaction. When Rh³⁺ ions are continuously consumed and drop to a critical value, the remaining Rh³⁺ ions

and thiourea repeat the stage I) and proceed copolymerization reaction on the surface of the core via Rh–S bonds to form the Rh/NSC shell. Finally, under heat treatment, compared with the shell with low Rh/NSC mass ratio, the evaporation rate and volatile products of the core are more pronounced, leading to the generation of voids and the formation of Rh/NSC yolk-shell structure. III) If the Rh/C mass ratio keeps increasing, the homogeneous nucleation of Rh³⁺ ions dominates the reaction in the whole process. Thiourea would then participate in the reaction through copolymerization with Rh³⁺ ions and acts as a structural indicator. Thus, after high-temperature carbonization treatment, a porous nanostructure is formed.

The HER electrocatalytic performance of Rh₁₅/NSC YSS was next evaluated via a typical three electrode system. For comparison, we have also included the data collected on Rh₅/NSC nanoparticles (NP), Rh₃₀/NSC porous particles (PP), commercial

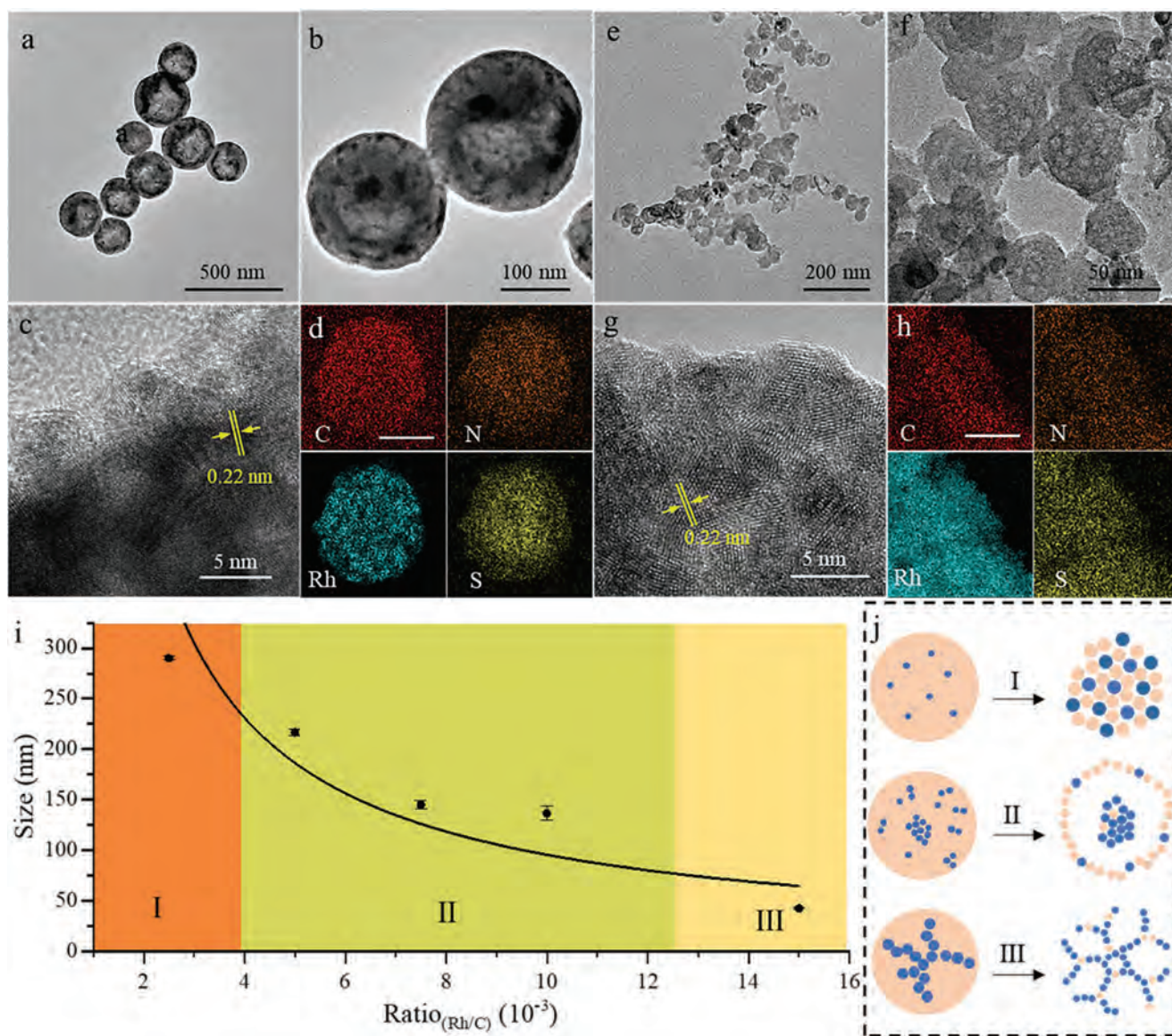


Figure 2. a,b) TEM images, c) HRTEM image and d) corresponding EDS mappings of the Rh₅/NSC NP. e,f) TEM images, g) HRTEM image and h) corresponding EDS mappings of the Rh₃₀/NSC PP. i) The plot of size versus ratio_(Rh/C). j) Schematic illustration of the nanostructure formation mechanism in different stages, including NP, YSS, and PP. Orange: carbon. Blue: Rh.

20% Pt/C and commercial 5% Rh/C (C-Rh/C). Among these five samples, Rh₁₅/NSC YSS exhibits the best electrocatalytic performance in the 1 M KOH electrolyte (pH = 14), with the lowest overpotential (13.5 mV at 10 mA cm⁻², **Figure 3a**) and Tafel slope (24.9 mV dec⁻¹, **Figure 3b**), which is better than those of commercial 20% Pt/C and outperforming the state-of-the-art HER electrocatalysts (**Figure 3c**, detailed values are summarized in Table S1, Supporting Information). Importantly, systematic studies based on experimental data and DFT calculations have proved that hydrogen binding energy (HBE) provides a key descriptor for HER activity.^[21,22] In order to evaluate the origin of the superior HER activity of Rh₁₅/NSC YSS, correlations were established between HER activities and experimentally measured HBE using the CV method under the corresponding electrochemical conditions. **Figure 3d** exhibits the CV curves

of Rh₅/NSC NP, Rh₁₅/NSC YSS, Rh₃₀/NSC PP, and commercial Pt/C in the 1 M KOH, which reveal well-defined patterns, including the adsorption/desorption of underpotential deposition hydrogen (H_{upd}) below 0.4 V (vs. reversible hydrogen electrode (RHE)) and wide double-layer potential region between 0.4 and 0.6 V (vs. RHE). Based on previous results, the potential of H_{upd} desorption peak (E_{peak}) could be directly related to the HBE of active site by $\Delta HBE = -FE_{\text{peak}}$ (F is Faraday constant), which yielded a superior HBE of -0.163 eV for Rh₁₅/NSC YSS as compared with that of Pt/C (-0.246 eV for Pt(110) and -0.356 eV for Pt(100)) in 1 M KOH.^[23] Thus, the enhanced HER intrinsic activity of Rh₁₅/NSC YSS can be ascribed to a weaker H chemisorption strength as compared to Pt/C, triggering the acceleration of the hydrogen desorption step. Meanwhile, with the assistance of X-ray photoelectron spectroscopy (XPS), when

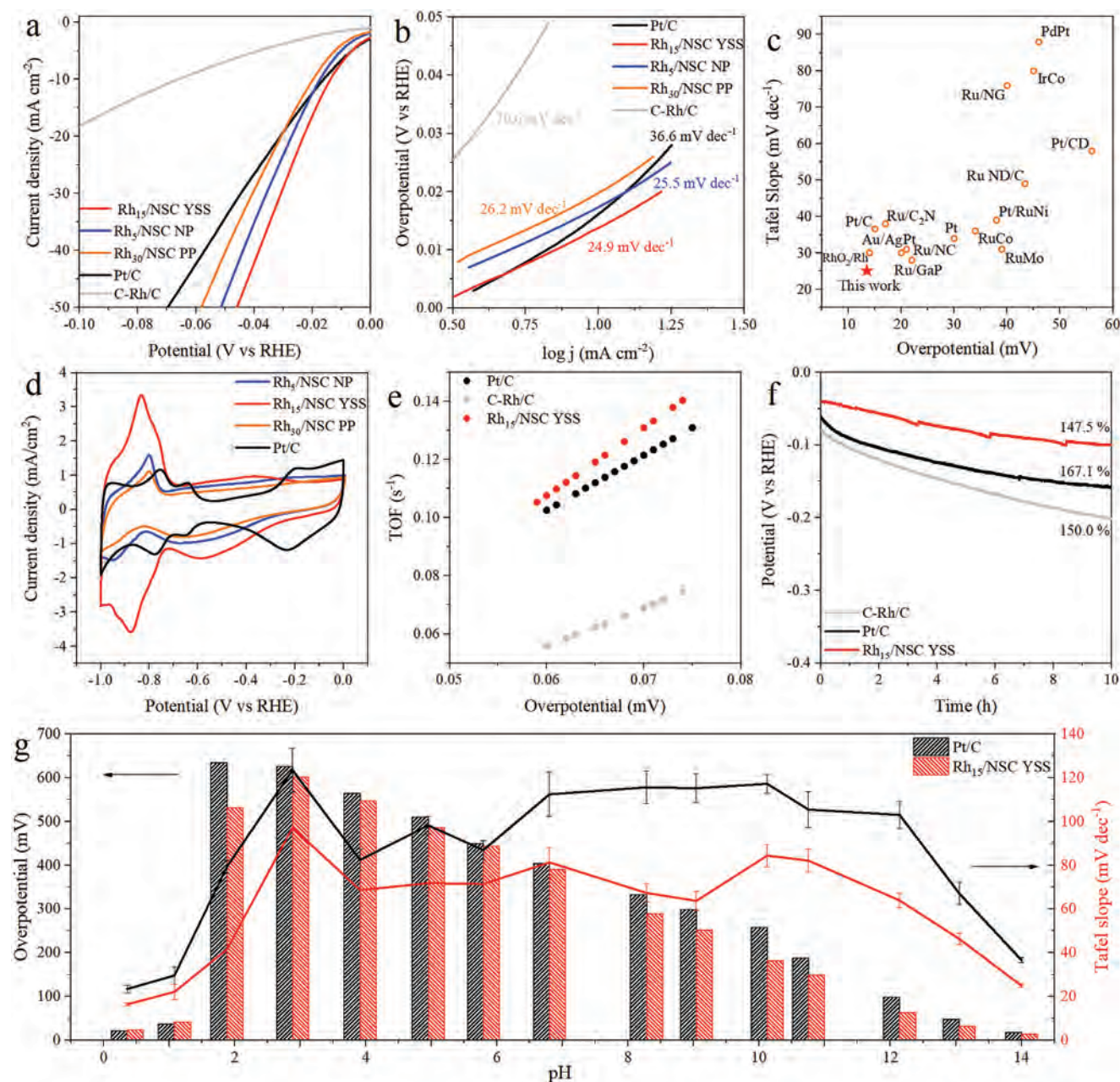


Figure 3. a) Polarization curves of the Rh₁₅/NSC YSS electrocatalyst in 1 M KOH with a scan rate of 5 mV s⁻¹, along with Rh₁₅/NSC NP, Rh₃₀/NSC PP, Pt/C and commercial Rh/C for comparison. (b) are the corresponding Tafel slope. (c) The electrocatalytic performance comparison among various noble metal-based materials in the 1 M KOH electrolyte. (d) Cyclic voltammograms tested in the range of 0 and 1 V (vs RHE). (e) TOF plots of the Rh₁₅/NSC YSS, Pt/C and commercial Rh/C. (f) Time-dependent current density plots versus time without iR correction at a static current density (10 mA cm⁻²). (g) The variation of Tafel slopes and over potential (10 mA cm⁻²) of Rh₁₅/NSC YSS and Pt/C catalysts with the pH values (0–14).

the Rh/C mass ratio increases, the change of the coordination environment of Rh (the covalent bonds formed between S and Rh and possible hydrogen bonds formed between N and Rh) results in the improvement of the percentage of oxidized Rh (located at 309.8 and 314.8 eV) (Figure S13, Supporting Information), indicating that the electronic structure of active sites can be controlled via changing the Rh/C mass ratio.

Moreover, electrochemical impedance spectroscopy (EIS) analyses of the catalysts have been employed to further understand the reaction kinetics for HER with the equivalent circuit

depicted in Figure S14 (Supporting Information). The semi-circles in the high-frequency range and low-frequency range are associated with charge-transfer resistance (R_{ct}) and mass-transfer resistance (R_{mt}), respectively.^[24] Among these three samples, Rh₁₅/NSC YSS exhibits the lowest R_{ct} (8.37 Ω) and R_{mt} (1.74 Ω), indicating a faster HER process (Figure S15, Supporting Information). The elements of the value in the equivalent circuit are summarized in Table S2 (Supporting Information). To evaluate the electrochemical surface area (ECSA) of the prepared catalysts, the electrochemical double-layer capacitances (C_{dl}) of

the catalysts are measured via a simple cyclic voltammetry (CV) method (Figure S16, Supporting Information).^[25] The Rh₁₅/NSC YSS exhibits the largely increased ECSA, which can be attributed to the optimized electronic structure of the Rh active centers. The mass activity is also considerable for evaluating the activity of electrocatalysts. As shown in Figure S17 (Supporting Information), it can be observed that the Rh₁₅/NSC YSS electrocatalyst requires a small overpotential of only 51 mV to attain a current density of 500 mA cm⁻² mg⁻¹, being much lower than the corresponding Rh₅/NSC NP and Rh₃₀/NSC PP catalysts, respectively. The intrinsic activities of electrocatalysts are then evaluated by the turnover frequency (TOF) by assuming all the noble metal atoms to be catalytically active.^[26] Among these samples, Rh₁₅/NSC YSS achieves the highest TOF of 0.143 s⁻¹ at the overpotential of 75 mV, which is larger than those of Pt/C (0.131 s⁻¹) and C-Rh/C (0.075 s⁻¹) (Figure 3e). Notably, the Rh₁₅/NSC YSS also displays long-term stability with a degradation rate of 147.5% during 10 h, which is better than the ones of Pt/C (161.7%) and C-Rh/C (150.0%), verifying the promotion effect of yolk-shell structure to stabilize architectural morphology and effectively avoids the coverage of active sites during reaction (Figure 3f). It should be noticed the slight degradation may be attributed to the existence of few RhO₂ layers on the surface. Previous reports has proved that the intrinsic HER activity of Rh oxides is higher than that of pure Rh.^[15] Thus, the activity loss is expected to be observed since RhO₂ is unstable and readily reduced into metallic states during the HER process. Then, the physical characterization results for reacted electrocatalysts demonstrated the stability of the yolk-shell structure and surface reconstruction phenomenon (Figure S18, Supporting Information). An ideal HER electrocatalyst should not only possess excellent performance in 1 M KOH electrolyte, but also exhibits high efficiency over a wide pH value, even at all pH values. The polarization curves of Rh₁₅/NSC YSS and Pt/C obtained for entire pH range are compiled in Figure S19 (Supporting Information) (acid condition), Figure S20 (Supporting Information) (neutral condition), and Figure S21 (Supporting Information) (alkaline condition). Figure 3g records the overpotential (current density is 10 mA cm⁻²) and corresponding Tafel slopes of the electrocatalysts in the whole pH range. In specific, Rh₁₅/NSC YSS shows a faster kinetic process than that of Pt/C in all the electrolyte of different pH values. Therefore, even in the strong acid condition (pH = 0.36 and 1.08) where the overpotential of Rh₁₅/NSC YSS exceeds that of Pt/C, Rh₁₅/NSC YSS still exhibits a higher electrocatalytic performance than Pt/C.

In addition to the electronic structure optimization of the Rh active sites, the unique yolk-shell structure is also considered to play an important role in the HER process. Surprisingly, the Rh₁₅/NSC YSS exhibits the best hydrophilicity among these three kinds of nanostructures that can be contributed to the existence of capillary force in the small voids. This way, this capillary force would significantly improve the electrolyte infiltration into the voids compared with NP and PP nanostructures, resulting in a smaller contact angle with electrolytes (Figure 4a–c). Also, the Rh₁₅/NSC YSS exhibits the excellent aerophobic property, which is beneficial for the H₂ desorption (Figure 4d–f). To gain a further insight into the effect of nanostructures on the HER performance, the gas bubbles release behavior is further investigated during the in situ

electrochemical process. Taking the HER recorded at -0.05 V (vs RHE) as an example, hydrogen bubbles escaped easily from the Rh₁₅/NSC YSS surface with a size of 28.7 ± 0.1 nm that are obviously smaller than those of Rh₅/NSC NP (36.0 ± 2.7 nm) and Rh₁₅/NSC PP (61.2 ± 2.1 nm) (Figure 4g–i). This phenomenon is closely related to the gas bubbles nucleation, transfer and desorption process. Specifically, for the Rh₅/NSC NP electrocatalyst, typical gas bubbles behavior is occurred on the surface. The bubbles nucleate and grow on the active sites, and after reaching the critical size, they will directly desorb and diffuse into the electrolyte (Figure 4j). While for the Rh₁₅/NSC YSS electrocatalyst, compared with the larger bubbles generated on the outer shell, more gas bubbles are quickly generated and restricted on the surface of the core part because of the spatial confinement effect and heterogeneous composition. Based on the Young–Laplace equation, $P_s = 2\gamma/R$, the pressure of a bubble is inversely proportional to its radius (P_s , γ and R present the pressure, surface tension coefficient and radius of curvature, respectively). The small gas bubbles inside can diffuse into the large bubbles easily through the shell because of the pressure difference, then bubbles on the outside will be quickly released.^[27] The ion transfer rate is positively correlated to the rate of gas escape; hence, the rapid desorption of gas bubbles for Rh₁₅/NSC YSS is beneficial for accelerating the catalytic reaction (Figure 4k). In addition, the generated gas bubbles on the inner surface of yolk-shell system would result in the difference in electrolyte concentration between the surface and the interior space. The presence of electrolyte concentration difference is a source of penetration pressure that facilitates rapid mass transfer at the interface, which is consistent with the EIS analysis. For the Rh₃₀/NSC PP electrocatalyst, the generated gas bubbles are easily trapped in the porous channel, covering the active sites and reducing the catalytic performance (Figure 4l).

3. Conclusion

In summary, heterogeneous Rh/S, N co-doped carbon electrocatalysts with yolk-shell nanostructures are successfully prepared by a facile self-template method. The optimized electrocatalyst can achieve an extremely small overpotential of 13.5 mV at 10 mA cm⁻², a low Tafel slope of 25.5 mV dec⁻¹, a high TOF of 0.143 s⁻¹ (at -75 mV per RHE) and long-term durability for 10 h, which is the best alkaline HER activity among the ever-reported noble metal based catalysts to the best of our understanding. More importantly, it also exhibits superior electrocatalytic activities at all pH, which is better than commercial Pt/C and Rh/C catalysts. These striking performance can be ascribed to the optimized electronic structure and unique yolk-shell structure. All these results demonstrate the Rh based nanomaterials as promising superior electrocatalysts in a wide pH range while the nanostructure design is a powerful tool to increase the mass/electron transfer during reaction.

4. Experimental Section

Preparation of Rh/C Yolk-Shell Nanospheres: Typically, 15 mg of RhCl₃ and 2 g of thiourea were dissolved in 10 mL of distilled water,

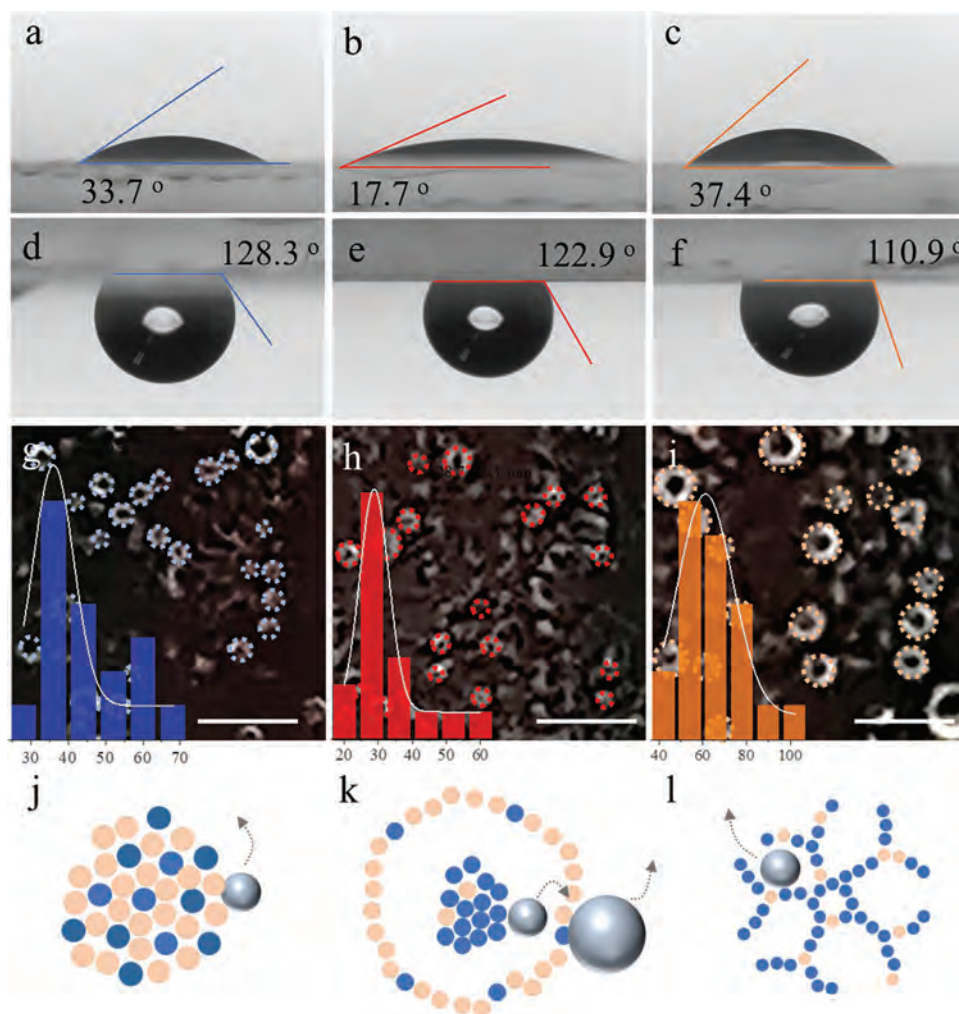


Figure 4. a–c) Images of the water contact angle measurement of 5 μL of 1 M KOH drop on the Rh₅/NSC NP, Rh₁₅/NSC YSS and Rh₃₀/NSC PP film. d–f) Images of the bubble contact angle measurement of 1 M KOH solution of Rh₅/NSC NP, Rh₁₅/NSC YSS and Rh₃₀/NSC PP film. g–i) Digital photos of the hydrogen bubbles produced on the surface of different samples during HER at -0.05 V versus RHE. Insets show the statistics on the gas bubble size distribution. All scale bars are 500 μm . j–l) Schematic illustration of the gas bubbles formation and release process on the surface of different electrocatalysts.

respectively. The RhCl₃ solution was then added to the thiourea solution slowly under stirring until the clear transparent solution was obtained. The mixture solution was sealed into a 35 mL Teflon-lined stainless steel autoclave reactor, which was next heated at 140 °C for 12 h in an electric oven. After cooling the system to room temperature naturally, the brown precipitates were gathered and washed several times with ethanol and deionized water by centrifugation, followed by vacuum dry at 60 °C overnight. Finally, the Rh₁₅/NSC YSS were transformed from brown precipitates by a heat treatment method in air atmosphere at 450 °C for 6 h with a heating rate of 2 °C min⁻¹. For comparison, Rh_x/NSC ($x = 5, 10, 20,$ and 30) electrocatalysts were prepared as control samples using the same methods except for changing the feeding amount of RhCl₃ for 5, 10, 20 and, 30 mg, respectively.

Characterization: The purity and crystalline structure of prepared samples were evaluated by powder X-ray diffraction (XRD) with a scan rate of 0.05° s⁻¹ in a 2 θ scan ranging from 20 to 90° using a Bruker D2 Phaser (Bruker, Billerica, MA, USA) instrument equipped with a monochromatic Cu-K α radiation. The morphology and dimension of obtained products were observed by scanning electron microscopy (SEM, Phenom Pro, Phenom-World, The Netherlands) with an accelerating voltage of 10 kV and field-emission SEM (SU-8010, Hitachi, Tokyo,

Japan) with an accelerating voltage of 15 kV. Water and gas contact angle were tested by Dataphysics Contact Angel Tester. Transmission electron microscopy (TEM) and high-resolution (HR) TEM were conducted by a Tecnai G² F30 (FEI, Hillsboro, or, USA) using an accelerating voltage of 200 kV. X-ray photoelectron spectroscopy (XPS) was performed with a VG Multilab 2000 (Thermo Fisher Scientific, Waltham, MA, USA) photoelectron spectrometer using a monochromatic Al-K α radiation under vacuum at a pressure of 2×10^{-6} Pa. All the binding energies were referenced to the C1s peak at 284.8 eV of the surface adventitious carbon.

Electrochemical Measurements: For electrochemical measurement, the well-dispersed catalyst ink was prepared by ultrasonication with 3 mg of fabricated electrocatalyst, 50 μL of distilled water, 170 μL of ethanol, 10 μL of Nafion for 2 h. Then, 5 μL of the catalyst ink was pipetted onto the glass carbon electrode surface (5 mm in diameter, $S = 0.19625$ cm²). All electrochemical characterization was investigated with a Gamry 300 electrochemical workstation connected with a standard three-electrode configuration under 25 °C using a constant temperature bath. The fabricated electrode sample was used as the working electrode. A saturated calomel electrode (SCE) and a carbon rod were employed as the reference electrode and counter electrode, respectively. All the reported

potentials were calibrated versus the reversible hydrogen electrode (RHE) using the equation of $E_{\text{RHE}} = E_{\text{SCE}} + (0.2415 + 0.059 \times \text{pH})$ V, where E_{RHE} is the potential referred to RHE and E_{SCE} is the measured potential against the SCE reference electrode. The electrochemical activity of the samples toward HER and OER were surveyed in 1 M KOH aqueous solution (pH = 14) by linear sweep voltammetry (LSV) at a scan rate of 5 mV s^{-1} . To keep the electrode surface in a relatively stable state, several cyclic voltammetry (CV) cycles were operated before the assessment of electrochemical activity until the hydrogen evolution currents showed the unnoticeable change. Unless otherwise mentioned, the voltammograms were recorded with the iR drop compensation automatically on the workstation. Electrochemical impedance spectroscopy (EIS) was conducted at 1.5 V (vs RHE) over a frequency range of between 0.05 Hz and 100 kHz at 5 mV s^{-1} . Turnover frequency (TOF) is calculated from the equation of $\text{TOF} = \frac{I \times A}{2 \times F \times n}$, where I is the current density, A is the exposed surface area of the electrocatalyst, F is the Faradic constant and n is the moles of the active materials. Herein, the noble metal atoms for each catalyst loaded on the glass carbon electrode are considered as active sites.

At the same time, the electrolyte was prepared as following: 0.5 M H_2SO_4 (pH = 0.36), 0.05 M H_2SO_4 + 0.45 M Na_2SO_4 (pH = 1.08), 5 mM H_2SO_4 + 0.49 M Na_2SO_4 (pH = 1.88), 0.5 mM H_2SO_4 + 0.49 M Na_2SO_4 (pH = 2.88), 0.05 mM H_2SO_4 + 0.49 M Na_2SO_4 (pH = 3.91), 5 mM H_2SO_4 + 0.49 M Na_2SO_4 (pH = 4.95), 0.5 mM H_2SO_4 + 0.49 M Na_2SO_4 (pH = 5.79), 0.5 M Na_2SO_4 (pH = 6.8), 1 M KOH (pH = 14), 0.1 M KOH + 0.6 M K_2SO_4 (pH = 13.05), 0.01 M KOH + 0.66 M K_2SO_4 (pH = 12.14), 1 mM KOH + 0.66 M K_2SO_4 (pH = 10.75), 0.1 mM KOH + 0.66 M K_2SO_4 (pH = 10.12), 0.01 mM KOH + 0.66 M K_2SO_4 (pH = 9.04), 1 mM KOH + 0.66 M K_2SO_4 (pH = 8.28). All pH range was covered in this investigation.

Supporting Information

Supporting Information is available from the Wiley Online Library or from the author.

Acknowledgements

This work was financially supported by the Environment and Conservation Fund of Hong Kong SAR, China (ECF 2020-13) and the City University of Hong Kong (project no. 9667227).

Conflict of Interest

The authors declare no conflict of interest.

Author Contributions

X.M.B. and Y.B. contributed equally to this work. X.M.B. and Y.B. conceived the idea and led the project. Q.Q., S.W.Y., Y.M. and D.C. processed the sample growth, structural characterization under the guidance of X.M.B., X.Y.W., and J.L., Z.X.L., P.S.X., D.Y. and D.J.L. processed the electrochemical measurements. J.C.H. validated the experimental results and performed data curation. X.M.B. and Y.B. cowrote the manuscript. All authors made revisions and gave approval to the manuscript.

Data Availability Statement

The data that support the findings of this study are available from the corresponding author upon reasonable request.

Keywords

full pH range, heterogeneous electrocatalysis, hydrogen evolution reactions, noble metals, yolk-shell structures

Received: May 26, 2022

Revised: June 17, 2022

Published online: July 8, 2022

- [1] X. Zou, Y. Zhang, *Chem. Soc. Rev.* **2015**, *44*, 5148.
- [2] M. Fang, G. Dong, R. Wei, J. C. Ho, *Adv. Energy Mater.* **2017**, *7*, 1700559.
- [3] X. Bu, Y. Li, J. C. Ho, *MRS Bull.* **2020**, *45*, 531.
- [4] A. Parra-Puerto, K. L. Ng, K. Fahy, A. E. Goode, M. P. Ryan, A. Kucernak, *ACS Catal.* **2019**, *9*, 11515.
- [5] J. Zhang, Q. Zhang, X. Feng, *Adv. Mater.* **2019**, *31*, 1808167.
- [6] M. F. Lagadec, A. Grimaud, *Nat. Mater.* **2020**, *19*, 1140.
- [7] X. Bu, R. Wei, W. Gao, C. Lan, J. C. Ho, *J. Mater. Chem. A* **2019**, *7*, 12325.
- [8] W. Tong, M. Forster, F. Dionigi, S. Dresp, R. Sadeghi Erami, P. Strasser, A. J. Cowan, P. Farràs, *Nat. Energy* **2020**, *5*, 367.
- [9] J. E. Bennett, *Int. J. Hydrogen Energy* **1980**, *5*, 401.
- [10] H. Xu, J. Wan, H. Zhang, L. Fang, L. Liu, Z. Huang, J. Li, X. Gu, Y. Wang, *Adv. Energy Mater.* **2018**, *8*, 1800575.
- [11] M. Fang, W. Gao, G. Dong, Z. Xia, S. P. Yip, Y. Qin, Y. Qu, J. C. Ho, *Nano Energy* **2016**, *27*, 247.
- [12] J. Yang, W. Li, S. Tan, K. Xu, Y. Wang, D. Wang, Y. Li, *Angew. Chemie – Int. Ed.* **2021**, *60*, 19085.
- [13] P. Zhu, X. Xiong, D. Wang, *Nano Res.* **2022**, *15*, 5792.
- [14] K. Wang, B. Huang, F. Lin, F. Lv, M. Luo, P. Zhou, Q. Liu, W. Zhang, C. Yang, Y. Tang, Y. Yang, W. Wang, H. Wang, S. Guo, *Adv. Energy Mater.* **2018**, *8*, 1801819.
- [15] Z. Li, Y. Feng, Y. L. Liang, C. Q. Cheng, C. K. Dong, H. Liu, X. W. Du, *Adv. Mater.* **2020**, *32*, 1908521.
- [16] J. N. Hansen, H. Prats, K. K. Toudahl, N. Mørch Secher, K. Chan, J. Kibsgaard, I. Chorkendorff, *ACS Energy Lett.* **2021**, *6*, 1175.
- [17] Z. W. She, J. Kibsgaard, C. F. Dickens, I. Chorkendorff, J. K. Nørskov, T. F. Jaramillo, *Science* **2017**, *355*, aad4998.
- [18] N. Danilovic, R. Subbaraman, D. Strmcnik, V. R. Stamenkovic, N. M. Markovic, *J. Serbian Chem. Soc.* **2013**, *78*, 2007.
- [19] Y. Y. Ma, C. X. Wu, X. J. Feng, H. Q. Tan, L. K. Yan, Y. Liu, Z. H. Kang, E. B. Wang, Y. G. Li, *Energy Environ. Sci.* **2017**, *10*, 788.
- [20] Y. Xiong, J. Dong, Z. Q. Huang, P. Xin, W. Chen, Y. Wang, Z. Li, Z. Jin, W. Xing, Z. Zhuang, J. Ye, X. Wei, R. Cao, L. Gu, S. Sun, L. Zhuang, X. Chen, H. Yang, C. Chen, Q. Peng, C. R. Chang, D. Wang, Y. Li, *Nat. Nanotechnol.* **2020**, *15*, 390.
- [21] J. K. Nørskov, T. Bligaard, A. Logadottir, J. R. Kitchin, J. G. Chen, S. Pandelov, U. Stimming, *Phys. Inorg. Chem.* **2005**, *152*, 23.
- [22] Q. Wang, C. Q. Xu, W. Liu, S. F. Hung, H. Bin Yang, J. Gao, W. Cai, H. M. Chen, J. Li, B. Liu, *Nat. Commun.* **2020**, *11*, 4246.
- [23] G. S. Karlberg, T. F. Jaramillo, E. Skúlason, J. Rossmeisl, T. Bligaard, J. K. Nørskov, *Phys. Rev. Lett.* **2007**, *99*, 126101.
- [24] H. Xia, Z. Huang, C. Lv, C. Zhang, *ACS Catal.* **2017**, *7*, 8205.
- [25] J. Zhang, W. Xiao, P. Xi, S. Xi, Y. Du, D. Gao, J. Ding, *ACS Energy Lett.* **2017**, *2*, 1022.
- [26] Y. Chen, H. Li, J. Wang, Y. Du, S. Xi, Y. Sun, M. Sherburne, J. W. Ager, A. C. Fisher, Z. J. Xu, *Nat. Commun.* **2019**, *10*, 572.
- [27] P. Hou, D. Li, N. Yang, J. Wan, C. Zhang, X. Zhang, H. Jiang, Q. Zhang, L. Gu, D. Wang, *Angew. Chemie – Int. Ed.* **2021**, *60*, 6926.